

# Machine Learning-Aided Crystal Facet Rational Design with Ionic Liquid Controllable Synthesis

Fuming Lai, Zhehao Sun, Sandra Elizabeth Saji, Yichuan He, Xuefeng Yu, Haitao Zhao,\* Haibo Guo,\* and Zongyou Yin\*

**Crystallographic facets in a crystal carry interior properties and proffer rich functionalities in a wide range of application areas. However, rational prediction, on-demand customization, and accurate synthesis of facets and facet junctions of a crystal are enormously desirable but still challenging. Herein, a framework of machine learning (ML)-aided crystal facet design with ionic liquid controllable synthesis is developed and then demonstrated with the star-material anatase TiO<sub>2</sub>. Aided by employing ML to acquire surface energies from facet junction datasource, the relationships between surface energy and growth conditions based on the Langmuir adsorption isotherm are unveiled, enabling to develop controllable facet synthetic strategies. These strategies are successfully verified after applied for synthesizing TiO<sub>2</sub> crystals with custom crystal facets and facet junctions under tuning ionic liquid [bmim][BF<sub>4</sub>] experimental conditions. Therefore, this innovative framework integrates data-intensive rational design and experimental controllable synthesis to develop and customize crystallographic facets and facet junctions. This proves the feasibility of an intelligent chemistry future to accelerate the discovery of facet-governed functional material candidates.**

Dr. F. Lai, Dr. X. Yu, Dr. H. Zhao  
Materials Interfaces Center  
Shenzhen Institutes of Advanced Technology  
Chinese Academy of Sciences  
Shenzhen 440305, China  
E-mail: ht.zhao@siat.ac.cn

Dr. F. Lai  
Jinhua Advanced Research Institute  
Jinhua 321019, China  
Z. Sun, S. E. Saji, Dr. Z. Yin  
Research School of Chemistry  
Australian National University  
Canberra, ACT 2601, Australia  
E-mail: Zongyou.Yin@anu.edu.au

Z. Sun, Y. He  
School of Energy and Power Engineering  
Dalian University of Technology  
Dalian 116024, China

Dr. H. Guo  
School of Materials Science and Engineering  
Shanghai University  
Shanghai 200444, China  
E-mail: guohaibo@shu.edu.cn

 The ORCID identification number(s) for the author(s) of this article can be found under <https://doi.org/10.1002/smll.202100024>.

DOI: [10.1002/smll.202100024](https://doi.org/10.1002/smll.202100024)

## 1. Introduction

The traditional research and development of functional materials are mainly based on the scientific intuition of researchers and a large number of repeated trial-and-error experiments, which are formidable tasks. Consequently, researchers made further efforts to develop a theoretical model to speed up the discovery of functional materials. Unfortunately, a large number of experimental and theoretical results have not been fully integrated and utilized. In 2011, the Materials Genome Initiative advanced a new paradigm for high-performance materials discovery and design to replace the standard trial-and-error approach.<sup>[1,2]</sup> At the same time, the databases containing varied crystal characteristics were presented to address the deficiency of experimental measurements.<sup>[3,4]</sup> An enormous amount of experimental and theoretical studies has been performed with making some

progress up to date.<sup>[5–8]</sup> This year, a novel robotic system for chemical synthesis was reported featured with a high-autonomous workflow<sup>[9]</sup> and hence automated synthesis is growing in popularity. The fourth paradigm (highly intelligent, data-intensive, and data-driven research) facilitated by the integration of machine learning (ML) algorithms and chemistry-related databases attracted more and more attention.<sup>[10–12]</sup> Therefore, data-driven experimental controllable synthesis has become a new pursuit to promote designing innovative materials with targeted properties for an intelligent chemistry future.

Facet in crystal morphology is one of the most important factors in determining the properties and performance of functional materials. For example, controlling and customizing crystal facets provide a promising potential in design and modification of some popular light-responsive semiconductors, greatly regulating the photocatalytic/photovoltaic properties,<sup>[13–16]</sup> for the applications in CO<sub>2</sub> reduction,<sup>[17,18]</sup> water splitting,<sup>[19–23]</sup> solar cells,<sup>[24]</sup> etc. Therefore, the controllable synthesis of targeted facets is critical for customizing materials functionalities and enhancing their performance in practical applications. Up to date, a wide range of applications of crystal facets, especially of low-dimensional nanomaterials, have been developed for the applications in energy conversion,<sup>[25–28]</sup> energy storage,<sup>[29]</sup> sensors,<sup>[30,31]</sup> organic pollutant removal,<sup>[32,33]</sup>

photovoltaic,<sup>[34]</sup> wettability<sup>[35]</sup> and so on. However, the accuracy of the experiment in controlling crystal facets is substantially difficult because of the various factors involved. In order to better understand morphological transformations of crystals in materials synthesis, the dependence of facets on crystal structures has been widely discussed. Some theories have been developed up to date, including Periodic Bond Chains theory,<sup>[36]</sup> Bravais–Friedel–Donnay–Harker law,<sup>[37]</sup> Harsh–Nidhi–Binay theory,<sup>[38]</sup> and so on. Unfortunately, most of them did not take experimental controllable synthesis into consideration and were unable to explain or predict various facet and hence their junctions in experiments.<sup>[17,19]</sup>

The need for producing targeted crystal facets and facet junctions, involved with complicated experimental growth conditions, is driving strong demand for rational theoretical modeling to predict the crystals and guide the controllable synthesis.<sup>[8,39]</sup> The relationship between crystal facets and experimental conditions is elaborated by considerable efforts but systematic understanding is still lacking.<sup>[40–42]</sup> An important part of the challenge is the lack of reliable, environment-dependent surface energies. All previous reports were focused on the Wulff constructions using first-principles to calculate the ideal surface energies for obtaining the facets of a given crystal. Surface energies, however, are elusive in both measurements and computations owing to highly complex environmental factors, such as temperature, pressure, concentration, and pH, that surround those volatile facets. In addition, most of the first-principles calculations are time consuming and limited to clean, low-index surfaces, and small surface cells. Thus, it is imperative to find a reasonable and efficient method to establish a relationship between the crystal facets (and hence facet junctions) and real surface energy that can integrate the material informatics to guide the experiment. To address this, a rational protocol design for artificial facets and facet junctions in light of ML-intensive methodology is expected. Actually, the success of computer-aided methods has inspired the development and application of artificial intelligence-based tools that contribute to reliable chemical synthesis.<sup>[4,6,43,44]</sup> Also, the latest advances in supervised and reinforced ML, such as artificial neural networks (ANN),<sup>[45–47]</sup> provide promising opportunities for accelerating synthesis and discovery of functional materials through ML-accelerated strategies.<sup>[48–50]</sup> Taking advantage of ML, an intelligent strategy is supposed to significantly accelerate the controllable synthesis for facet-governed crystals.

In this study, we propose a data-intensive rational design and controllable synthesis strategy, which integrates data-driven ML and ionic liquid experimental synthesis for crystal facets design. First, we provide an overview of the integrated framework toward artificial facet junctions of crystal. Then, we introduce the role of ML in the construction of the relationship between facets and surface energy. Next, the proposed data-driven ML is applied to backtrack surface energies from experimentally observed equilibrium morphologies. Moreover, taking anatase TiO<sub>2</sub> as a proof-of-concept study, our developed rational design of crystal facets and facet junctions is well demonstrated with synthesizing TiO<sub>2</sub> crystals, controlled via an ionic liquid [bmim][BF<sub>4</sub>].

## 2. Results and Discussion

### 2.1. Framework toward Artificial Facet Junction Design of a Crystal

Herein, we create a framework to bridge the facet junction data-source, ML, mathematical model, and ionic liquid synthesis and hence to achieve the rational design and controllable synthesis for the targetted functional materials featured with customized crystallographic facets and facet junctions. As shown in Figure 1, our procedures of framework integrate the following components and enable ML-aided crystal facet rational design with ionic liquid controllable synthesis to realize artificial facet junction of a crystal: i) an ML datasource containing abundant potential facets and facet junctions; ii) definition of a crystallographic path, iii) facet junctions customization for TiO<sub>2</sub> as an example, iv) ML-aided crystal facet rational design, and v) ionic liquid controllable synthesis.

For the first step, to implement the system, we built ML datasource based on the Wulff construction as an automation platform for further design. To generate a search space for facets and facet junctions as ML datasource, for the first step, we obtained 1075 different facets from seven crystal systems containing crystal informatics from the Materials Project,<sup>[2]</sup> which can construct about 2<sup>251</sup> potential morphologies and 92 033 different facet junctions for future facet rational design (see Figure 1a and the Supporting Information). A number of the candidate facets, morphologies, and facet junctions found here have already been validated by literature experiments, which suggest that the unstudied candidates unveiled in this work offer the valued datasource for further investigations. Next, to verify the proposed framework's applicability, in step 2, we have investigated surface energies of anatase-phase TiO<sub>2</sub> as an example for a proof-of-concept, to determine growth conditions for a given crystallographic path. The crystal structure of anatase TiO<sub>2</sub> is of the 4/mmm point group in the tetragonal crystal system. Nanocrystals in this point group include anatase,<sup>[25,51,52]</sup> rutile,<sup>[53]</sup> pyrolusite,<sup>[54,55]</sup> zircon,<sup>[56]</sup> etc. We considered {100}, {101}, {111}, and {001} facets here since the theoretical and experimental studies on surfaces of the 4/mmm point group mainly focus on low-index {100}, {101}, {111}, and {001} facets. In addition, we also considered the high index {103} facets to enrich the morphologies. Crystals of the tetragonal 4/mmm point group can be crystallized into various morphologies, such as octahedral,<sup>[57]</sup> cuboid,<sup>[58]</sup> truncated octahedral,<sup>[25]</sup> tetragonal faceted-nanorod,<sup>[52,59]</sup> and so on (Figure 1a). In this study, we take the {101} facets as the reference facets and express other surface energies as dimensionless ratios with respect to {101} facets. The numerical solutions of surface energy ratios for each polyhedron are presented in Step 2, through the constrained optimization by linear approximations (COBYLA) algorithm<sup>[60]</sup> in the nonlinear optimization (NLOpt) library (see Table S2, Supporting Information). Figure 1b shows the schematic model of the facet junction customization evolution when only five typical surfaces {101}, {100}, {001}, {103}, and {111} are considered for this point group. As the relative surface-energy ratio  $\gamma_{hkl}/\gamma_{101}$  changes, one or more types of facets appear or disappear. Crystal particles tend to grow fast along the normal direction of high-energy facets, often

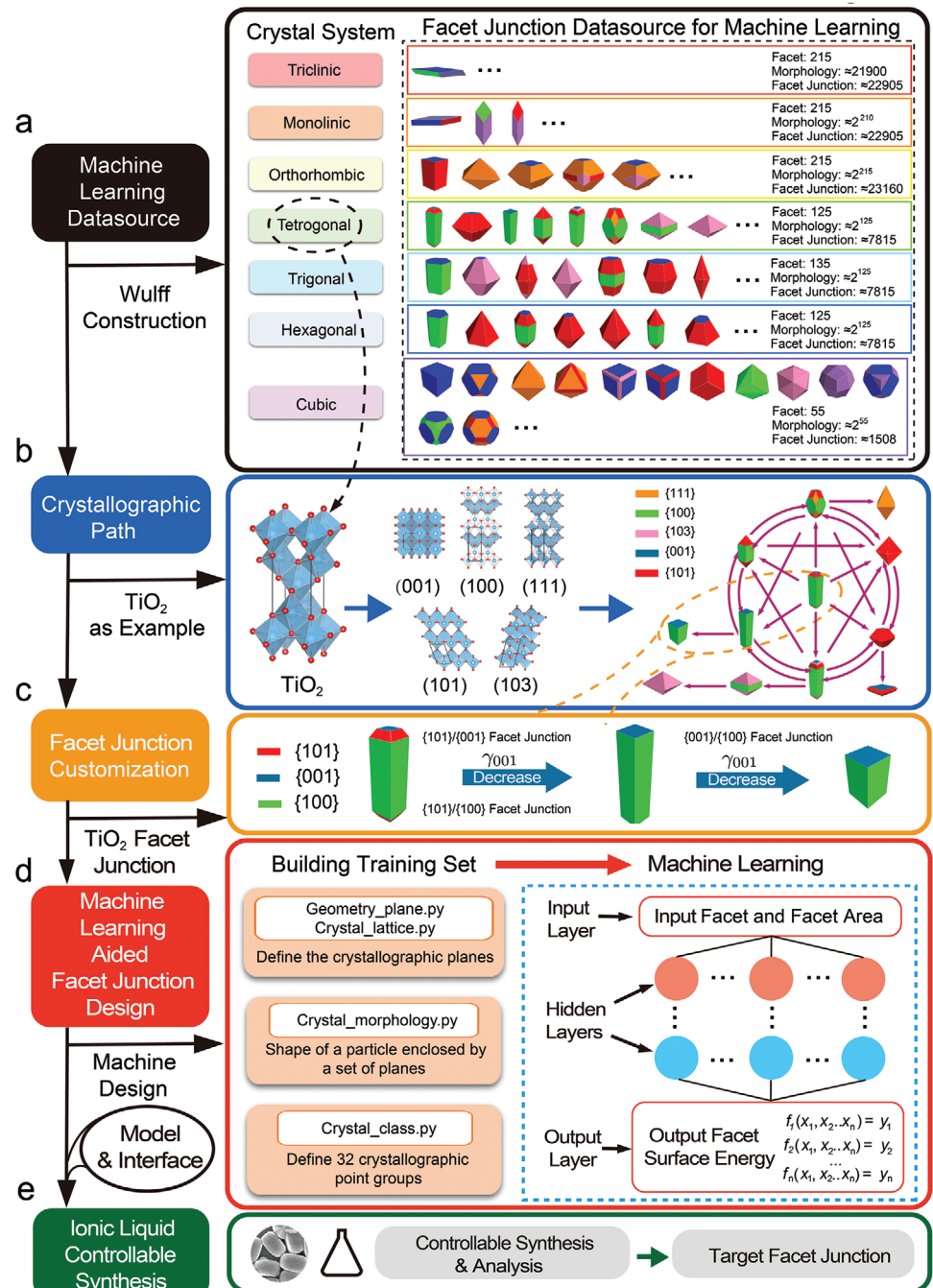


**Figure 1.** Framework toward artificial facet junctions of crystal. a) ML datasource based on Wulff construction. The number of facets, morphologies, and facet junctions for each crystal system is shown on the rightmost side (see Table S1, Supporting Information). b) The crystallographic path toward the tetragonal crystal system for  $\text{TiO}_2$  (as an example). c) Customization of  $\text{TiO}_2$  facet junction. d) The preprocess of training sets and ANN for ML aided facet junction rational design. e) The controllable synthesis performed by the ionic liquid.

eliminating high-energy facets and maximizing surface area of low-energy facets. Starting from a tetragonal faceted nanorod (in Figure 1c), one of the most thermodynamically stable form, at least six distinct shapes can be produced by decreasing (or increasing) the relevant surface energies. Here, in step 3, we customize anatase  $\text{TiO}_2$  crystals with a high percentage

of  $\{001\}$  facets and  $\{001\}/\{100\}$  facet as our target facet and facet junction, respectively, as shown in Figure 1c. Moreover, besides the tetragonal faceted-nanorod shape in the center of Figure 1b, various morphologies can be synthesized experimentally through adjusting various reaction conditions, i.e., temperature, pH, time, concentration, and ligand, during the

whole synthesis process to modify the relative surface energies. From the end of step 3, the framework has completed the crystal facet rational predesign preparations.

To correlate the surface energy with morphology modulation of a crystal, ML-aided crystal facet rational design was demonstrated in step 4. In our previous studies, surface energies calculated by the inverse Wulff construction method (see the Supporting Information) were discrete. To solve this deficiency, in step 4, our system further developed an ML integrated development strategy that facilitates to accelerate facet rational design using the ANN (see the Supporting Information). For crystals with more complex facets, ANN could be inspected and enhanced by the user through optimizing the network to improve the training efficiency and accuracy. In Figure 1d, we designed a set of calculation programs to obtain the training set, thereby allowing processes to be specified at an increasingly automated level. In order to build the training set, our calculation programs were considered as the interface for further machine training. To execute ML, we use an automatic processing program to calculate surface energies from experimentally observed particle morphologies through algorithms of minimization based on the ML datasource. The obtained surface energies are compatible with the real growth experimental conditions. In addition, the ML-aided method can be employed to supplement experimental observations since the calculated surface energies can be extrapolated to experimental conditions that have not been explored.<sup>[61]</sup> This allows one to compile a data set for energy-condition or even morphology-condition relationships with a small number of experiments.

After step 4, data-driven ML-aided rational design for crystal facet urgently needs to build a connecting relationship between the adjacent controllable synthetic steps. To solve this issue, we introduced ionic liquid controllable synthesis under the guidance of data in step 4 of Figure 1e. The controllable synthesis of functional materials was realized by varying the pH of the solution, concentration of ionic liquids, reaction temperature, and reaction time. As a typical solution-based parameter, the ionic liquid under hydrothermal condition has the stabilizing role for formed nanoparticles as a soft template or a capping agent and has proven to be an effective and convenient way in preparing various materials with diverse controllable morphologies. To verify the proposed strategy's applicability, we have used it to investigate surface energies of anatase-phase TiO<sub>2</sub> (of the 4/mmm point group) as an example, to determine growth conditions for a target crystal facet.

## 2.2. Machine Learning for Surface Energy Calculations

When the synthesis process takes advantage of ML-aided crystal facet rational design, it can provide a data-driven way to speed up the construction of relationships between facet and surface energy. In this study, the neural network of ML we used consists of an input layer, an output layer, and three hidden layers as shown in Figure 2a. However, a more complex selection of neural networks can be used in principle to improve the possibility of customization and optimization. The proposed facet junction (the area of facets) is taken as the descriptors and the surface energy of facets is considered as the target properties.

The input vector contains the elemental fractions normalized to one and the regression gives the output. The model learns to capture the required relationship among the facets from the input training data. We use three hidden layers to train all possible morphology data containing three facets in Figure S3 in the Supporting Information. Through regression testing, we choose hyperbolic tangent sigmoid transfer function as transfer function for each hidden layer, and the number of neurons is 3 in the input layer and 4, 4, and 4 in three hidden layers, which have been tested to show a better performance of regression (Tables S3 and S4 in the Supporting Information). For other morphologies of other materials, additional tests are required. The successfully trained neural network can already accurately predict the data of all possible morphologies of the three facets for TiO<sub>2</sub> (Figure S3, Supporting Information), so it can also predict the specific morphological path of the three facets in Figure 2c,d with high R<sup>2</sup>. As shown in Figure 2b, we use 1000 cases as the data sets and randomly split the data sets into training and test sets in the ratio of 8:2 for reporting the performance of ANN models. The data in this work are randomly selected from datasource considering all reasonable ranges of the morphology. Our training set and test set are randomly distributed. To take the surface energy ratio of facet {001}/{101} as an example, all the data of the training set and test set are shown in Figure S2 in the Supporting Information. Figure 2c,d illustrate the scatter plot of ANN models trained from preprocessed data sets. We find that the ML predicted values are well matched to that calculated by inverse Wulff construction; that is, ML leads to the accuracy with exhibiting low mean absolute errors (MAE) in the prediction of surface energy for facet junction. In addition, Figure S3 in the Supporting Information is the result of all the possible complex morphologies included of {001}, {101}, and {100} facets. This will result in multiple surface areas corresponding to the same surface energy ratio, thus sacrificing the accuracy. Specifically, the two green dot lines in Figure S3b,c in the Supporting Information indicate the specific ranges which are, respectively, the same as that presented in Figure 2c,d. After comparing these two specific ranges, it is obvious that the results of ML prediction is much more accurate, if we only consider the specific morphology path in Figure 2c,d, which has been experimentally demonstrated in this work. Besides, the predicted surface energies for four facets by ML reflects a more complicated situation, and ML can still accurately predict the relationship between the surface energy and the area of the facet shown in Figure S4 in the Supporting Information.

Next, a comparison between the ANN model and high accuracy solution is performed to predict surface-energy ratios as a function of morphology evolution. We demonstrate the internal representation for both of them in Figure 3a,b. The surface energies are calculated by the inverse Wulff construction method and can be used to fit a continuous function, which is

$$\gamma = (1-x) \left( a_0 - a_1 \sqrt{\frac{x}{(a_0-1)x+1}} + \frac{x}{a_2 - a_3 \sqrt{\frac{1-x}{(a_2-1)(1-x)+1}}} \right) \quad (1)$$

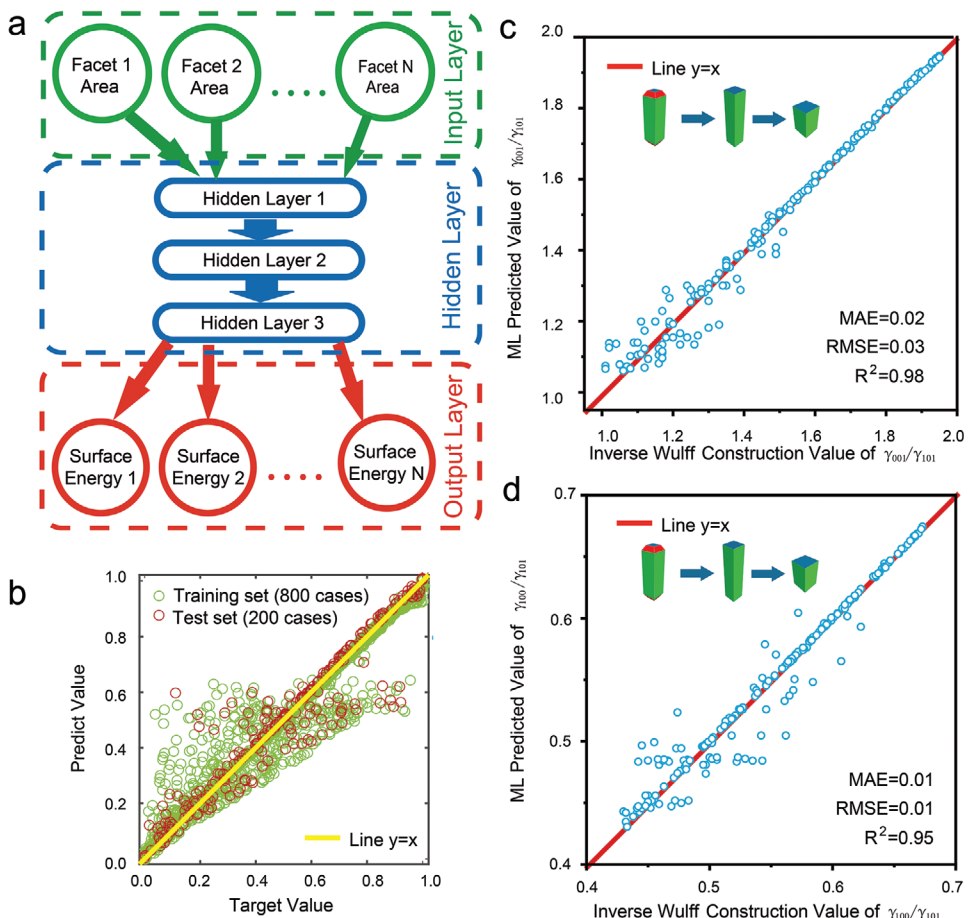


**Figure 2.** The convergence of facet surface energies for ML model. a) The scheme used for the training and application of the model. b) Scatter plot for iterations of the convergence system. The model was trained on the set of 800 cases and tested on the set of 200 cases. Facet surface energies for c)  $\{001\}/\{101\}$  facet junction and d)  $\{100\}/\{101\}$  facet junction are calculated using inverse Wulff construction and predicted using ML for specific morphological variation paths. Note: MAE means mean absolute error, RMSE means root mean squared error, and  $R^2$  means R-square.

where  $a_0$ ,  $a_1$ ,  $a_2$  and  $a_3$  are unknowns to be obtained from fitting.<sup>[61]</sup> The parameters of the fitting function are listed in Table S5 in the Supporting Information. In the present work, the shape from Figure 1c is considered one of the most desirable pathways for crystals of point group 4/mmm. This pathway can be divided into two stages. The first stage is where  $\{101\}$  facets disappear completely. The second stage is combined with an increasing fractional area of  $\{001\}$  and a decreasing fractional area of  $\{100\}$ . By fitting discrete numerical values of energy ratios to Equation (1), we are able to measure the energy ratios for any given fractional areas conveniently. In this way, we do not need the numerical optimization method, and this reduces the computational complexity. Though the inverse Wulff construction could obtain a high-accuracy solution, it needs to choose a suitable optimization algorithm (shown in Figure 3b), and it takes a very long time to calculate the surface energy for the morphology enclosed by multiple crystal facets (shown in Table S6 and S7, Supporting Information). As shown in Figure 3c,d, we observe that the model has a low prediction error compared with inverse Wulff construction calculated results. Under the condition of the same accuracy, we have demonstrated the efficacy of ML that could save much time (only in seconds) to accelerate

the crystal facet rational design compared with performing inverse Wulff construction.

### 2.3. Ionic liquid Aided Anatase-Phase Controllable Synthesis

We have used ML to automatically obtain the surface-energy ratios as a function of morphology evolution. To further model the underlying relationship between surface energy and growth conditions, ionic liquid aided anatase-phase controllable synthesis is designed to verify ML-aided crystal facet rational design. The functional relationship between surface energy and ion concentration is  $\gamma = e_0 \ln(1 + ce_1) + e_2$ . According to the function relation, the function is monotonously decreasing. Therefore, the greater the concentration results in the lower the surface energy, so the larger the area of the exposed surface could be obtained. This also shows that we want to get a larger  $\{001\}$  exposed surface, we must add more fluoride ion. Before the experiment, our model can already provide preliminary guidance for the experiment, but we do not know how much fluoride ions should be added. If we want to know what the specific functional relationship is, we need to determine the parameters  $e_0$ ,  $e_1$ , and  $e_2$ , which must be determined through experiments.

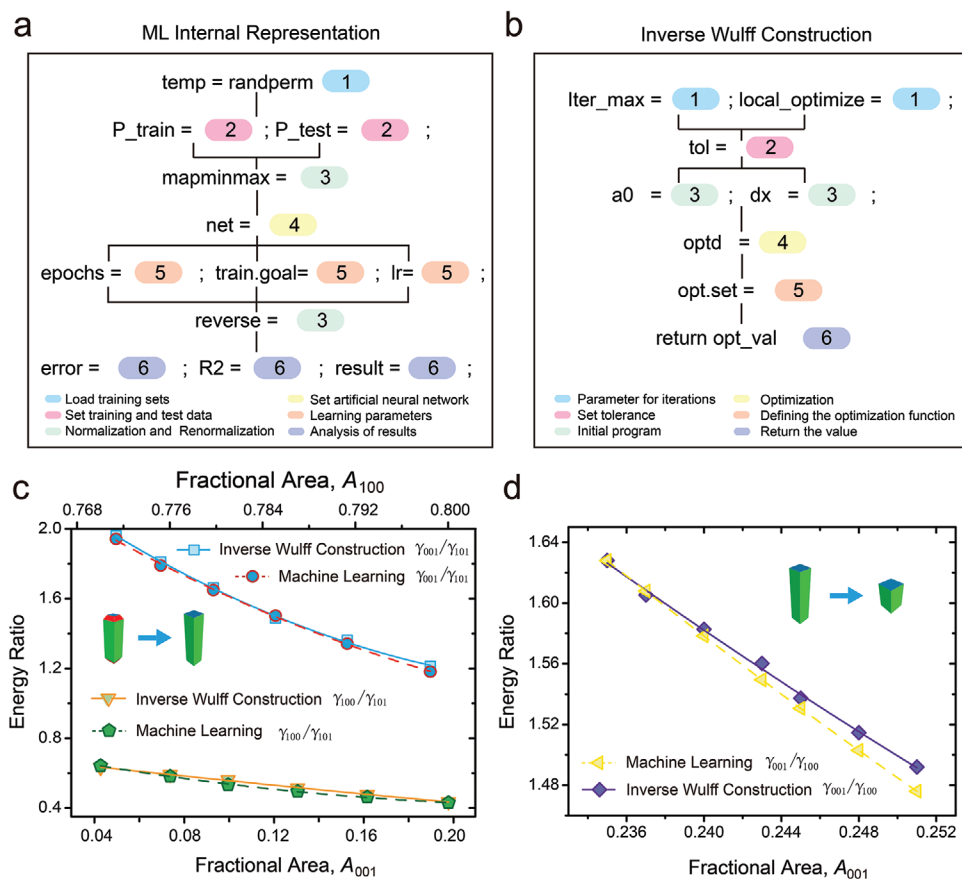


**Figure 3.** a) ML internal representation and b) inverse Wulff construction propagate data from steps to substeps. The fitting curves of surface-energy ratios as a function of morphology evolution. c) Tetragonal faceted-nanorod and d) cuboid with different aspect ratios. The comparison of results calculated by inverse Wulff construction and by ML shows the accuracy of ML prediction.

Because there are three parameters, at least three sets of experiments should be done. To exemplify the process, the controllable synthesis of anatase TiO<sub>2</sub> has been detailed, which was synthesized using the hydrothermal method with different amounts of [bmim][BF<sub>4</sub>] (see the Supporting Information). The X-ray diffraction (XRD) patterns of the as-synthesized sample with the amount of 1000 μL ionic liquid [bmim][BF<sub>4</sub>] is shown in Figure 4a. All diffraction peaks match well with the crystal structure of the anatase TiO<sub>2</sub> phase (space group *I41/amd*, Joint Committee on Powder Diffraction Standards (JCPDS) 21-1272) and no other phases can be detected, indicating that the product is in a pure anatase phase. Figure 4b,c shows the transmission electron microscopy (TEM) images of TiO<sub>2</sub> nanocuboids. The TEM image in Figure 4c clearly shows the (200) and (004) atomic planes with a lattice spacing of 0.19 and 0.24 nm, respectively. We can conclude that the anatase TiO<sub>2</sub> single crystals are bound by four {100} facets on four sides and two {001} facets on the top and bottom. Figure 4d–i displays scanning electron microscopy (SEM) images of TiO<sub>2</sub> crystals synthesized with different amounts of ionic liquid [bmim][BF<sub>4</sub>]. All the other parameters are the same. It can be found that the size of TiO<sub>2</sub> particles increases gradually with the increase of ionic liquid [bmim][BF<sub>4</sub>] amount, and only a fraction of the particles may be qualified as crystals, others being of the micrometer scale. The 3D morphology of well-faceted anatase TiO<sub>2</sub> nanocuboids is enclosed by two {001} top facets and four {100} lateral facets.

The TiO<sub>2</sub> crystals were synthesized with well-defined {001}/{100} facet junction and were shown that their shapes were affected by the amount of ionic liquid [bmim][BF<sub>4</sub>], which results in variations in the size of the {001} and {100} truncation facets in anatase and in the aspect ratio of crystals. It was also observed from a considerable amount of computational and experimental studies, that the presence of F<sup>-</sup> results in a large percentage area of anatase {001} facets by saturating surface unsaturated coordinated Ti<sub>5c</sub> atoms.<sup>[25,62]</sup> In our experiments, the F<sup>-</sup> ions are produced through the hydrolysis of [BF<sub>4</sub>]<sup>-</sup>. This is supported by the appearance of [BF<sub>4</sub>]<sup>-</sup>, which can effectively stabilize the {001} facets of anatase TiO<sub>2</sub>, and does not affect the appearance of {100} facets.<sup>[58]</sup> The surface energy of {100} facets is assumed to be constant. We may use Equation (7) to describe the surface-energy ratio  $\gamma_{001}/\gamma_{100}$ , which has been varied by adjusting the concentration of F<sup>-</sup> between 0.257 and 1.457 mol L<sup>-1</sup>. That is to say, Equation (7) that is applicable to a single surface is also tenable to describe a surface-energy ratio in this case.

To further demonstrate the feasibility of our model to execute ionic liquid aided controllable synthesis, we demonstrate the comparison of our model and experimental results. Figure 5a shows the aspect ratios and frictional surface areas of {001} facets. It can be seen that with the increase of ionic liquid [bmim][BF<sub>4</sub>] amounts, the aspect ratios increase gradually and the areas of {001} facets increase correspondingly. This is in

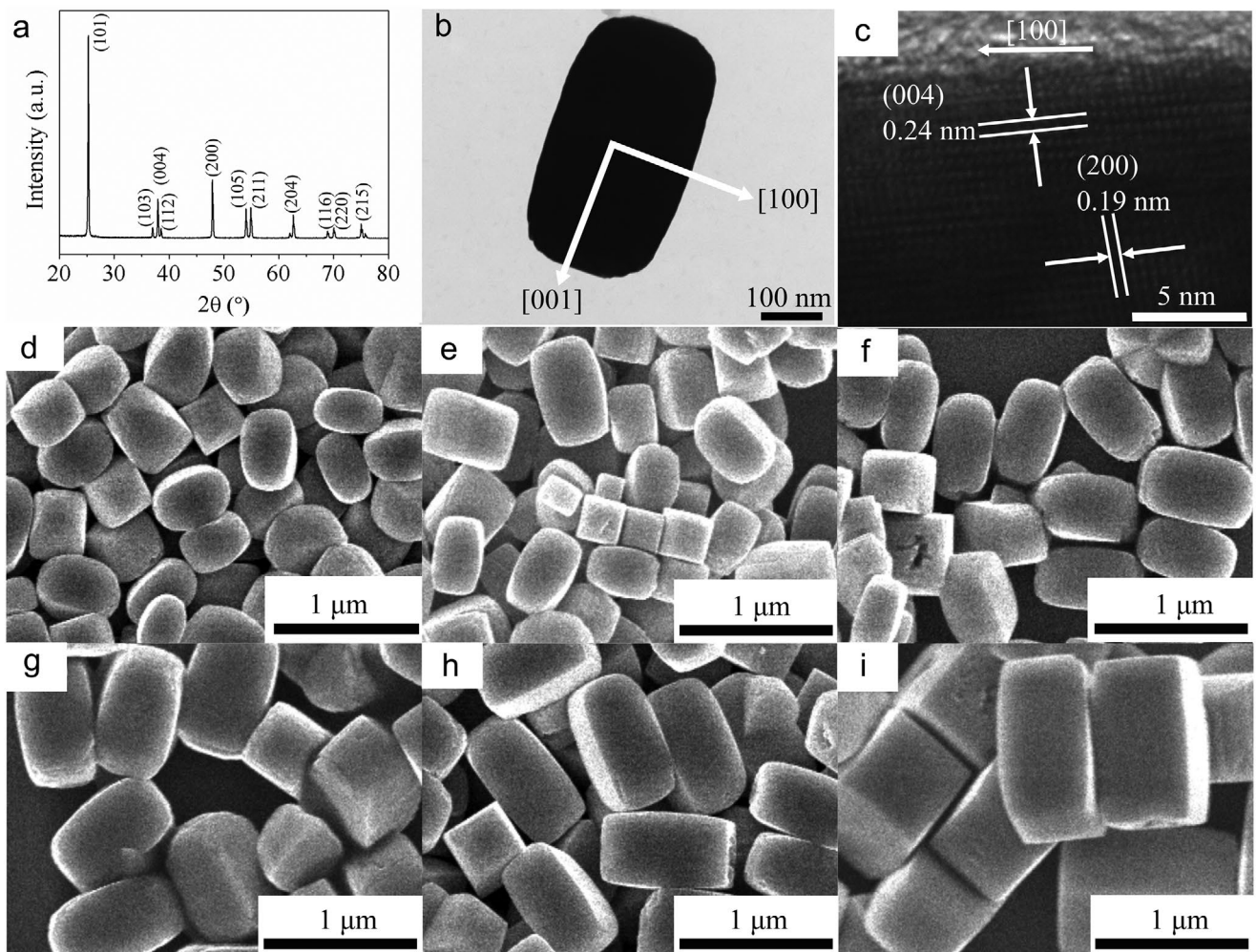


**Figure 4.** a) XRD patterns of  $\text{TiO}_2$  nanocrystals with a mount of 1000  $\mu\text{L}$  ionic liquid [bmim][BF<sub>4</sub>]. b,c), TEM images. SEM images of  $\text{TiO}_2$  nanocrystals synthesized with different amounts of ionic liquid [bmim][BF<sub>4</sub>]: d) 250  $\mu\text{L}$ , e) 500  $\mu\text{L}$ , f) 750  $\mu\text{L}$ , g) 1000  $\mu\text{L}$ , h) 1250  $\mu\text{L}$ , and i) 1500  $\mu\text{L}$ .

agreement with the finding that  $\text{F}^-$  can significantly reduce the surface energy of the {001} facets.<sup>[25]</sup> Besides, in Figure 5b, the surface-energy ratios are in accordance with the function in Equation (7) and the parameters are calculated by fitting the data for the four different concentrations of  $\text{F}^-$ . The value of  $\gamma_{001}/\gamma_{100}$  changes from 1.625 to 1.494 as the concentration of  $\text{F}^-$  changes from 0.257 to 1.457 mol L<sup>-1</sup>. It shows clearly that the fitting curve well matches the surface-energy ratios obtained from experimentally observed shapes of the  $\text{TiO}_2$  particles. In addition, by extending the concentration of  $\text{F}^-$  from 0.100 to 2.320 mol L<sup>-1</sup>, we are able to reproduce the surface-energy ratios at the concentrations of  $\text{F}^-$  and predict equilibrium particle shapes under these conditions. The lower surface-energy ratios in our experiments show that a higher percentage of {001} facets can be acquired by increasing the reaction temperature. The results in Figure 5b reveal the quantitative relationship between surface energy and morphology, surface energy, and fluoride ion concentration and indirectly established the relationship between morphology and fluoride ion concentration. Although only six sets of experiments are given in the paper, for other morphologies, the amount of fluoride ion can

be given according to the results of our model, which directly provides guidance for the experiment. The crystal structure of {100} and {001} facets for  $\text{TiO}_2$  is shown in Figure 5c. The results obtained from the experiments and numerical calculations allow us to propose a mechanism for understanding the relationship between datasource, ML, ionic liquid, and facet junction, as shown in Figure 5d.

For Figure 5d, the initial states is the construction of facet junctions datasource for ML, which is obtained by Wulff construction based on the Materials Project database<sup>[2]</sup> as an automation platform for  $\text{TiO}_2$  design. Then, ML is used to acquire surface energies from datasource of  $\text{TiO}_2$  crystal morphologies. ML in this work does not stop at calculating the surface energy of the theoretical model. It participates in the calculation of the surface energy of the experimental morphology. In addition, we have developed a model based on the Langmuir adsorption isotherm for surface energy as a function of ion concentration. Only when the surface energy is obtained, can the relationship between the surface energy and the ionic liquid be established, thereby achieving the purpose of controllable synthesis. Next, based on the surface energies

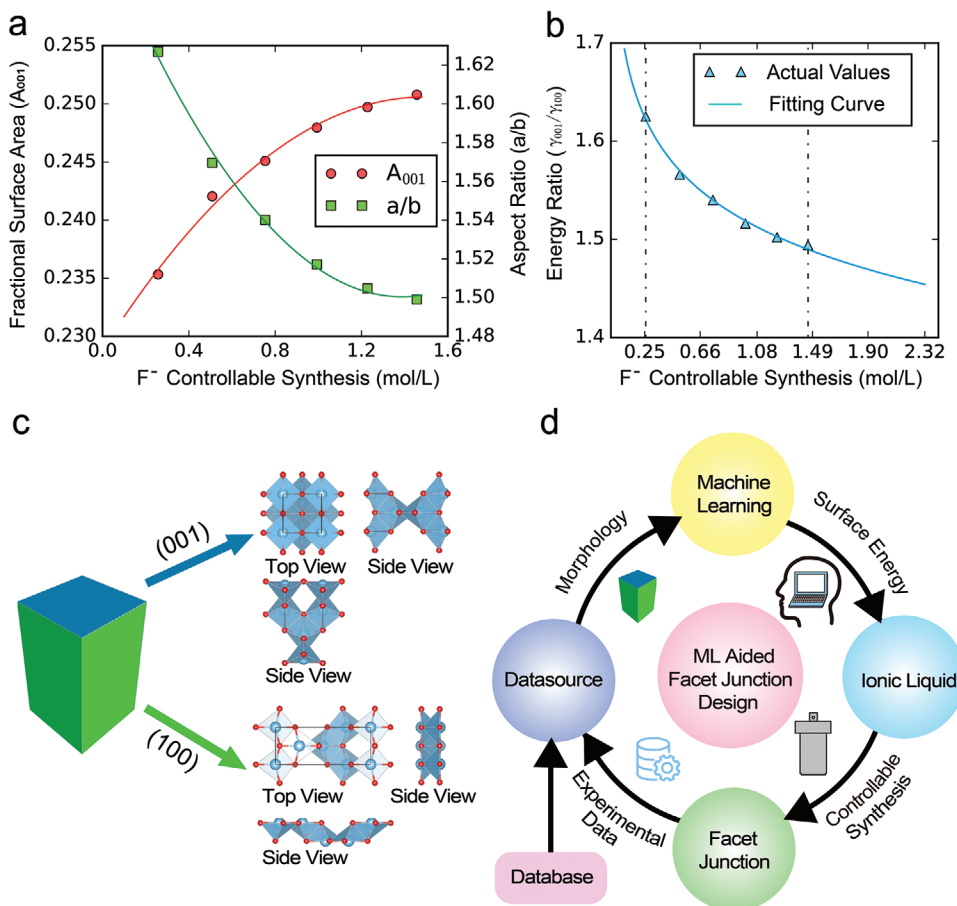


**Figure 5.** ML aided rational design for facet junctions: a) structural information of the TiO<sub>2</sub> samples prepared at different amounts of ionic liquid [bmim][BF<sub>4</sub>].  $a/b$  is the aspect ratio, where  $a$  and  $b$  are the length and width of TiO<sub>2</sub> nanocuboid, respectively.  $A_{001}$  is the fractional surface area of {001} facets. b) Fitting curve between surface-energy ratios and concentration of F<sup>-</sup> ranging from 0.257 to 1.457 mol L<sup>-1</sup>. The values of parameters  $e_0$ ,  $e_1$ , and  $e_2$  are -0.080 J m<sup>-2</sup>, 916.623 L mol<sup>-1</sup>, and 2.061 J m<sup>-2</sup>, respectively, which are deduced from the fittings. c) The present crystal structure of {100} and {001} facets for TiO<sub>2</sub> and d) framework for the ML aided facet junction design.

obtained through ML, the controllable synthesis of the target TiO<sub>2</sub> crystal facet junction is performed using an ionic liquid. Anatase TiO<sub>2</sub> crystals with a high percentage {001} facets and target {001}/{100} facet junction are successfully achieved. Finally, the morphological data of the experiment can be converted into our datasource (morphologies of six experimental points are shown in Table S8, Supporting Information), which will enrich our datasource. In addition, for a future perspective, if a high-throughput synthesis of facet and facet junctions with ionic liquid is achieved, experimental data can be set up as a new facet and facet junction experimental database. The integration of facet junction, ML guidance, and ionic liquid accelerates the design of ionic liquid controllable synthesis for specific crystallographic facets and facet junctions with a descriptor morphology relationship.

### 3. Conclusion

In this work, we presented a framework of machine learning-aided crystal facet rational design with ionic liquid controllable synthesis. This framework combines the material datasource,

machine learning, mathematical model, and ionic liquid experimental synthesis to realize the artificial facet junctions of crystals. The framework considered 1075 different facets from seven crystal systems, which can construct about 2<sup>251</sup> potential morphologies and 92 033 different facet junctions. Our datasource of materials offers an automation platform for crystal facet design and our data-driven ML integrated methodology can effectively calculate surface energies of crystals with various morphologies. In addition, we have developed a model based on the Langmuir adsorption isotherm for surface energy as a function of ion concentration. As a whole, such a framework allows for expert-aided guidance to develop rational strategies for the controllable synthesis of desirable crystals with customized facets and facet junctions. To synthesize the anatase-phase TiO<sub>2</sub> crystals, as an example, has been successfully performed to demonstrate the strategies by revealing the corelationships between crystal morphologies and the concentration of F<sup>-</sup>. A morphology-condition map can be set up with a small number of experiments and can be extrapolated to a large number of unexplored experimental conditions. Our workflow demonstrates avenues toward the rational design of specific crystallographic facets and facet junctions, which bridges data-intensive discoveries and experimental

strategies with the feasibility of intelligent chemistry. The strategy of ML-aided crystal facet rational design with ionic liquid controllable synthesis provides a way to accelerate synthesis and discovery of functional crystal facet junctions, toward the industry of facet-governed technologies.

#### 4. Experimental Section

*Inverse Wulff Construction:* The facet junctions of a crystal under or near equilibrium conditions are governed mainly by surface energies and the relationships between surface energy and experimental conditions can be predicted by mathematic models. In crystallography, the most thermodynamically stable particle shape has minimum total surface energy which is defined as

$$\Delta_f = \sum_i \gamma_i A_i \quad (2)$$

where  $\gamma_i$  and  $A_i$  are respectively the surface energies and areas of the  $i$ th surface. The corresponding equilibrium crystal morphology is theoretically described by the Wulff construction,<sup>[63–65]</sup> which minimizes the total surface energy at a constant volume. The Wulff construction revolutionized Geology and Crystallography and is widely used to determine crystal morphologies. Ding<sup>[66]</sup> was the first to generalize the Wulff construction to curved surfaces. Recently, Ringe et al.<sup>[67]</sup> presented the modified Wulff construction that can be used to predict the shape of twinned crystals. However, both the Wulff construction and its extensions need the values of surface energies to be known. Other thermodynamic models may also need surface energies of materials as input parameters.<sup>[61]</sup> However, measuring or calculating surface energies is difficult; instead, scanning and transmission electron microscopy techniques allowed to reliably quantify the nanocrystals' equilibrium shapes. Based on this analysis, a new approach was proposed for calculating the surface energy from experimentally observed equilibrium crystal shapes. The approach is a generalization of inverse Wulff construction,<sup>[61,68]</sup> in which surface energies are functions of areas of all exposing surfaces, as  $\gamma(A_1, A_2, \dots, A_n)$ . The unknown surface energies are to be solved by minimizing the total surface energy

$$\Delta_f = \sum_i A_i \gamma_i (A_1, A_2, \dots, A_n) \quad (3)$$

The underlying optimization algorithms are from the NLOpt library, which contains over 20 nonlinear algorithms for both local and global optimization.<sup>[60]</sup> All calculations in this work were carried out by the computer program.

*Dependence of Surface-Free Energy on Concentration:* Surface free energy is very sensitive to various experimental factors in a growth environment. In solution-mediated growth environments, concentration is a common and controllable parameter, and it can be taken as a representative to investigate the effect of experimental conditions on surface free energies. Gibbs derived a thermodynamic relationship between the concentration  $c$  and the surface excess  $\Gamma$  (adsorption per unit area). At constant temperature  $T$ , in the presence of adsorption, the Gibbs adsorption isotherm<sup>[69,70]</sup> is

$$\Gamma = -\frac{c}{RT} \frac{\partial \gamma}{\partial c} \quad (4)$$

where  $R$  is the universal gas constant and  $\gamma$  is the surface tension. In a chemical reaction, the surface excess is usually evaluated on the basis of the Langmuir adsorption model,<sup>[71–73]</sup> which has the form of

$$\Gamma = \Gamma_s \frac{ac}{1+ac} \quad (5)$$

where  $\Gamma_s$  saturated adsorption and  $a$  the Langmuir constant. Combining Equations (4) and (5), it is

$$\gamma = -\Gamma_s RT \ln(1+ac) + \text{const} \quad (6)$$

Furthermore, Equation (6) can be rewritten in a generalized form as

$$\gamma = e_0 \ln(1+ce_1) + e_2 \quad (7)$$

where  $e_0$ ,  $e_1$ , and  $e_2$  are parameters that are to be obtained from fitting.

It is to be noted that Equation (7) is applicable to surface tension, which differs by definition from free energy. Since the surface energy and surface tension are numerically equal for liquid's and isotropic solid's surfaces,<sup>[74]</sup> it was decided to ignore such a difference and treat the  $\gamma$  in Equation (7) as surface energy.

*Machine Learning Method:* Herein, an interface was employed to connect the relationship between facet junctions and their surface energies to accelerate the facet junction design toward ML. The subsequent analysis was based on ANN models as implemented in MATLAB and Simulink package. Identifying easily accessible and relevant functions was an integral part of any statistical learning activity. Since it is of the interest to learn the facets of different materials, structure information was chosen to uniquely represent the characteristics of different materials, which were easy to obtain. A database named the Materials Project was used to capture the materials informatic as the input in the preprocessing program. The training data originated from the output of the preprocessing program were initialized randomly from a uniform distribution. The areas of facets were used as descriptors and the surface energy of facets were the target properties. Because the area of the facet and the surface energy of each crystal was hardly evaluated simultaneously, the input vector contained the elemental fractions normalized to one and the regression gave the output of renormalization. ANN was used with an initial learning rate of 0.0001 during later epochs for convergence. It took several seconds to finish the training illustrated in this work, which saved much time compared with the ones based on inverse Wulff construction. The datasets used in this work are available with open access by using the following link: <https://github.com/Fuming-Lai/Training-Datasets>.

*Experimental Method:* Titanium dioxide ( $\text{TiO}_2$ )<sup>[25,51,52]</sup> was chosen since it is a well-known multifunctional material and was extensively studied owing to its broad applications. Its photocatalytic and photoelectrochemical performances were sensitive to morphologies of its nanostructures. In this work, anatase  $\text{TiO}_2$  crystals of cuboid shapes with  $\{100\}/\{001\}$  facet junction, which was one of the most important morphologies for photocatalysis and photoelectrochemistry, were synthesized and analyzed to provide necessary inputs for the inverse Wulff construction method. It was reported that, in hydrothermal synthesis experiments, cuboid-shaped  $\text{TiO}_2$  crystals were formed when fluorine ions were present in the hydrothermal solution.<sup>[58]</sup> The resultant cuboids' aspect ratios changed with the  $\text{F}^-$  concentrations. The detailed procedures in the synthesis experiments have been provided in the Supporting Information.

*Synthesis of Cuboid Anatase  $\text{TiO}_2$  Crystals:* All the chemicals in the experiments were of analytical grade and were used as received without further purification. Nanoscale anatase  $\text{TiO}_2$  was synthesized by a hydrothermal route using titanium tetraisopropoxide (TTIP), acetic acid (HAc), deionized water, and the ionic liquid 1-butyl-3-methylimidazolium tetrafluoroborate ( $[\text{bmim}]^+[\text{BF}_4]^-$ ) with different mole ratios as the precursor. TTIP and  $[\text{bmim}]^+[\text{BF}_4]^-$  serve as titanium and fluorine sources, respectively. In a typical synthesis, 20 mL acetic acid (HAc), 50  $\mu\text{L}$  deionized water, and a certain amount of ionic liquid  $[\text{bmim}]^+[\text{BF}_4]^-$  were mixed within a Teflon-lined autoclave with a capacity of 50 mL. After being stirred for a few minutes, TTIP (500  $\mu\text{L}$ ) was introduced dropwise into the mixture under stirring. Samples obtained from different contents of ionic liquid  $[\text{bmim}]^+[\text{BF}_4]^-$  were labeled as F- $c$ , where  $c$  represents the content of ionic liquid  $[\text{bmim}]^+[\text{BF}_4]^-$  ( $c = 250, 500, 750, 1000, 1250, 1500 \mu\text{L}$ ). In sequence, these obtained milky suspensions were heated in an electric oven at 200 °C for 36 h. After cooling to room temperature, the products were collected by centrifugation, washed with ethanol several times, and dried at 60 °C in an oven for 12 h. The morphology and crystalline structure of the samples were characterized by a field emission scanning electron microscope (JEOL, JSM-7500F), XRD (Rigaku D/max-2500, Cu-K radiation), and TEM (JEOL, JEM-2100F, 200 kV).

## Supporting Information

Supporting Information is available from the Wiley Online Library or from the author.

## Acknowledgements

F.L. and Z.S. contributed equally to this work. This work was supported by the National Natural Science Foundation of China (Nos. 51706114 and 51302166), Functional Materials Interfaces Genome (FIG) project, Doctoral Fund of Ministry of Education of China (20133108120021), the Australian National University (ANU) Future Scheme (Q4601024), and the Australian Research Council (DP190100295 and LE190100014).

## Conflict of Interest

The authors declare no conflict of interest.

## Data Availability Statement

The data that support the findings of this study are available from the corresponding author upon reasonable request.

## Keywords

controllable synthesis, crystal facets, ionic liquids, machine learning, rational design

Received: January 3, 2021

Revised: February 2, 2021

Published online: March 3, 2021

- [1] J. J. de Pablo, N. E. Jackson, M. A. Webb, L. Q. Chen, J. E. Moore, D. Morgan, R. Jacobs, T. Pollock, D. G. Schlom, E. S. Toberer, J. Analytis, I. Dabo, D. M. DeLongchamp, G. A. Fiete, G. M. Grason, G. Hautier, Y. Mo, K. Rajan, E. J. Reed, E. Rodriguez, V. Stevanovic, J. Suntivich, K. Thornton, J. C. Zhao, *npj Comput. Mater.* **2019**, 5, 41.
- [2] A. Jain, S. P. Ong, G. Hautier, W. Chen, W. D. Richards, S. Dacek, S. Cholia, D. Gunter, D. Skinner, G. Ceder, K. A. Persson, *APL Mater.* **2013**, 1, 011002.
- [3] L. Zhang, B. He, Q. Zhao, Z. Zou, S. Chi, P. Mi, A. Ye, Y. Li, D. Wang, M. Avdeev, S. Adams, S. Shi, *Adv. Funct. Mater.* **2020**, 30, 2003087.
- [4] D. Jha, K. Choudhary, F. Tavazza, W. keng Liao, A. Choudhary, C. Campbell, A. Agrawal, *Nat. Commun.* **2019**, 10, 5316.
- [5] C. Chen, Y. Zuo, W. Ye, X. Li, Z. Deng, S. P. Ong, *Adv. Energy Mater.* **2020**, 10, 1903242.
- [6] P. Chen, Z. Tang, Z. Zeng, X. Hu, L. Xiao, Y. Liu, X. Qian, C. Deng, R. Huang, J. Zhang, Y. Bi, R. Lin, Y. Zhou, H. Liao, D. Zhou, C. Wang, W. Lin, *Matter* **2020**, 2, 1651.
- [7] B. Mikulak-Klucznik, P. Gołębierska, A. A. Bayly, O. Popik, T. Klucznik, S. Szymkuć, E. P. Gajewska, P. Dittwald, O. Staszewska-Krajewska, W. Beker, T. Badowski, K. A. Scheidt, K. Molga, J. Mlynarski, M. Mrksich, B. A. Grzybowski, *Nature* **2020**, 588, 83.
- [8] Z. Zhang, J. A. Schott, M. Liu, H. Chen, X. Lu, B. G. Sumpter, J. Fu, S. Dai, *Angew. Chem., Int. Ed.* **2019**, 58, 259.
- [9] S. H. M. Mehr, M. Craven, A. I. Leonov, G. Keenan, L. Cronin, *Science* **2020**, 370, 101.
- [10] R. W. Epps, M. S. Bowen, A. A. Volk, K. Abdel-Latif, S. Han, K. G. Reyes, A. Amassian, M. Abolhasani, *Adv. Mater.* **2020**, 32, 2001626.
- [11] V. L. Deringer, C. J. Pickard, D. M. Proserpio, *Angew. Chem., Int. Ed.* **2020**, 59, 15880.
- [12] A. O. Oliynyk, A. Mar, *Acc. Chem. Res.* **2018**, 51, 59.
- [13] R. Li, F. Zhang, D. Wang, J. Yang, M. Li, J. Zhu, X. Zhou, H. Han, C. Li, *Nat. Commun.* **2013**, 4, 1432.
- [14] R. Chen, S. Pang, H. An, J. Zhu, S. Ye, Y. Gao, F. Fan, C. Li, *Nat. Energy* **2018**, 3, 655.
- [15] G. Liu, J. C. Yu, G. Q. Lu, H. M. Cheng, *Chem. Commun.* **2011**, 47, 6763.
- [16] Y. Bi, S. Ouyang, N. Umezawa, J. Cao, J. Ye, *J. Am. Chem. Soc.* **2011**, 133, 6490.
- [17] F. Chen, H. Huang, L. Ye, T. Zhang, Y. Zhang, X. Han, T. Ma, *Adv. Funct. Mater.* **2018**, 28, 1804284.
- [18] C. Zhou, S. Wang, Z. Zhao, Z. Shi, S. Yan, Z. Zou, *Adv. Funct. Mater.* **2018**, 28, 1801214.
- [19] A. Y. Zhang, W. Y. Wang, J. J. Chen, C. Liu, Q. X. Li, X. Zhang, W. W. Li, Y. Si, H. Q. Yu, *Energy Environ. Sci.* **2018**, 11, 1444.
- [20] S. Wang, G. Liu, L. Wang, *Chem. Rev.* **2019**, 119, 5192.
- [21] S. Bai, X. Li, Q. Kong, R. Long, C. Wang, J. Jiang, Y. Xiong, *Adv. Mater.* **2015**, 27, 3444.
- [22] T. Takata, J. Jiang, Y. Sakata, M. Nakabayashi, N. Shibata, V. Nandal, K. Seki, T. Hisatomi, K. Domen, *Nature* **2020**, 581, 411.
- [23] X. Hu, S. Lu, J. Tian, N. Wei, X. Song, X. Wang, H. Cui, *Appl. Catal., B* **2019**, 241, 329.
- [24] J. Yu, J. Fan, K. Lv, *Nanoscale* **2010**, 2, 2144.
- [25] H. G. Yang, C. H. Sun, S. Z. Qiao, J. Zou, G. Liu, S. C. Smith, H. M. Cheng, G. Q. Lu, *Nature* **2008**, 453, 638.
- [26] N. Uddin, H. Zhang, Y. Du, G. Jia, S. Wang, Z. Yin, *Adv. Mater.* **2020**, 32, 1905739.
- [27] Z. Yin, Z. Wang, Y. Du, X. Qi, Y. Huang, C. Xue, H. Zhang, *Adv. Mater.* **2012**, 24, 5374.
- [28] L. Wang, W. Chen, D. Zhang, Y. Du, R. Arnal, S. Qiao, J. Wu, Z. Yin, *Chem. Soc. Rev.* **2019**, 48, 5310.
- [29] J. S. Chen, Y. L. Tan, C. M. Li, Y. L. Cheah, D. Luan, S. Madhavi, F. Y. C. Boey, L. A. Archer, X. W. (David) Lou, *J. Am. Chem. Soc.* **2010**, 132, 6124.
- [30] R. Zhang, T. Zhou, L. Wang, T. Zhang, *ACS Appl. Mater. Interfaces* **2018**, 10, 9765.
- [31] X. Han, M. Jin, S. Xie, Q. Kuang, Z. Jiang, Y. Jiang, Z. Xie, L. Zheng, *Angew. Chem., Int. Ed.* **2009**, 48, 9180.
- [32] J. Li, C. Xiao, K. Wang, Y. Li, G. Zhang, *Environ. Sci. Technol.* **2019**, 53, 11023.
- [33] X. Ren, Y. Liu, W. Guo, *Sep. Purif. Technol.* **2020**, 253, 117501.
- [34] S. Y. Leblebici, L. Leppert, Y. Li, S. E. Reyes-Lillo, S. Wickenburg, E. Wong, J. Lee, M. Melli, D. Ziegler, D. K. Angell, D. F. Ogletree, P. D. Ashby, F. M. Toma, J. B. Neaton, I. D. Sharp, A. Weber-Bargioni, *Nat. Energy* **2016**, 1, 16093.
- [35] Z. Zhu, Z. Yu, F. F. Yun, D. Pan, Y. Tian, L. Jiang, X. Wang, *Natl. Sci. Rev.* **2020**, 7, 1.
- [36] P. Hartman, W. G. Perdok, *Acta Crystallogr.* **1955**, 8, 525.
- [37] R. Docherty, G. Clydesdale, K. J. Roberts, P. Bennema, *J. Phys. D: Appl. Phys.* **1991**, 24, 89.
- [38] H. Yadav, N. Sinha, B. Kumar, *Cryst. Growth Des.* **2016**, 16, 4559.
- [39] J. Zhao, X. Cheng, G. Zhao, Y. Lu, Y. Wang, H. Wang, H. Chen, *Chem. Commun.* **2019**, 55, 5571.
- [40] W. C. Huang, L. M. Lyu, Y. C. Yang, M. H. Huang, *J. Am. Chem. Soc.* **2012**, 134, 1261.
- [41] H. Guo, A. S. Barnard, *J. Mater. Chem. A* **2013**, 1, 27.
- [42] M. W. Anderson, J. T. Gebbie-Rayet, A. R. Hill, N. Farida, M. P. Attfield, P. Cubillas, V. A. Blatov, D. M. Proserpio, D. Akporiaye, B. Arstad, J. D. Gale, *Nature* **2017**, 544, 456.

- [43] M. A. Mosquera, B. Fu, K. L. Kohlstedt, G. C. Schatz, M. A. Ratner, *ACS Energy Lett.* **2018**, 3, 155.
- [44] J. Schmidt, M. R. G. Marques, S. Botti, M. A. L. Marques, *npj Comput. Mater.* **2019**, 5, 83.
- [45] M. Chen, U. Challita, W. Saad, C. Yin, M. Debbah, *IEEE Commun. Surv. Tutorials* **2019**, 21, 3039.
- [46] A. K. Jain, J. Mao, K. M. Mohiuddin, *Computer* **1996**, 29, 31.
- [47] J. J. Devogelaer, H. Meekes, P. Tinnemans, E. Vlieg, R. de Gelder, *Angew. Chem., Int. Ed.* **2020**, 59, 21711.
- [48] T. Toyao, Z. Maeno, S. Takakusagi, T. Kamachi, I. Takigawa, K. I. Shimizu, *ACS Catal.* **2020**, 10, 2260.
- [49] J. P. Janet, F. Liu, A. Nandy, C. Duan, T. Yang, S. Lin, H. J. Kulik, *Inorg. Chem.* **2019**, 58, 10592.
- [50] J. Noh, J. Kim, H. S. Stein, B. Sanchez-Lengeling, J. M. Gregoire, A. Aspuru-Guzik, Y. Jung, *Matter* **2019**, 1, 1370.
- [51] C. Byrne, L. Moran, D. Hermosilla, N. Merayo, Á. Blanco, S. Rhatigan, S. Hinder, P. Ganguly, M. Nolan, S. C. Pillai, *Appl. Catal., B* **2019**, 246, 266.
- [52] J. Li, D. Xu, *Chem. Commun.* **2010**, 46, 2301.
- [53] Z. Lai, F. Peng, H. Wang, H. Yu, S. Zhang, H. Zhao, *J. Mater. Chem. A* **2013**, 1, 4182.
- [54] W. Wei, X. Cui, W. Chen, D. G. Ivey, *Chem. Soc. Rev.* **2011**, 40, 1697.
- [55] K. Chen, C. Sun, D. Xue, *Phys. Chem. Chem. Phys.* **2015**, 17, 732.
- [56] G. Vavra, *Contrib. Miner. Petrol.* **1994**, 117, 331.
- [57] K. C. Lee, S. Sreekantan, Z. A. Ahmad, K. A. Saharudin, M. A. A. Taib, *CrystEngComm* **2017**, 19, 6406.
- [58] X. Zhao, W. Jin, J. Cai, J. Ye, Z. Li, Y. Ma, J. Xie, L. Qi, *Adv. Funct. Mater.* **2011**, 21, 3554.
- [59] M. Synowiec, A. Micek-Ilnicka, K. Szczepanowicz, A. Rózycka, A. Trenczek-Zajac, K. Zakrzewska, M. Radecka, *Appl. Surf. Sci.* **2019**, 473, 603.
- [60] S. G. Johnson, The NLOpt Non-Linear Optimisation Package, <http://ab-initio.mit.edu/nlopt> (accessed: November 2013).
- [61] F. Lai, Y. Chen, H. Guo, *J. Cryst. Growth* **2019**, 508, 1.
- [62] Y. Liu, *J. Appl. Crystallogr.* **2018**, 51, 1237.
- [63] F. Jiang, L. Yang, D. Zhou, G. He, J. Zhou, F. Wang, Z. G. Chen, *Appl. Surf. Sci.* **2018**, 436, 989.
- [64] G. Wulff, *Z. Kristallogr. - Cryst. Mater.* **1901**, 34, 449.
- [65] H. Guo, A. S. Barnard, *J. Mater. Chem.* **2011**, 21, 11566.
- [66] A. Dinghas, *Z. Kristallogr.* **1944**, 105, 304.
- [67] E. Ringe, R. P. Van Duyne, L. D. Marks, *J. Phys. Chem. C* **2013**, 117, 15859.
- [68] M. Giesen, C. Steimer, H. Ibach, *Surf. Sci.* **2001**, 471, 80.
- [69] G. Scatchard, *J. Phys. Chem.* **1962**, 66, 618.
- [70] L. Martínez-Balbuena, A. Arteaga-Jiménez, E. Hernández-Zapata, C. Márquez-Beltrán, *Adv. Colloid Interface Sci.* **2017**, 247, 178.
- [71] I. Langmuir, *J. Am. Chem. Soc.* **1918**, 40, 1361.
- [72] K. S. Park, Z. Ni, A. P. Cote, J. Y. Choi, R. Huang, F. J. Uribe-Romo, H. K. Chae, M. O'Keeffe, O. M. Yaghi, *Proc. Natl. Acad. Sci.* **2006**, 103, 10186.
- [73] X. Wang, S. Yu, Y. Wu, H. Pang, S. Yu, Z. Chen, J. Hou, A. Alsaedi, T. Hayat, S. Wang, *Chem. Eng. J.* **2018**, 342, 321.
- [74] A. S. Barnard, P. Zapol, *J. Chem. Phys.* **2004**, 121, 4276.